Journal of ELECTRONIC MATERIALS, Vol. 45, No. 1, 2016
DOI: 10.1007/s11664-015-4125-6

Influence of Ce-Substitution on Structural, Magnetic and Electrical Properties of Cobalt Ferrite Nanoparticles

A. HASHHASH[1,2,3] and M. KAISER[1]

1.—Reactor Physics Department, Nuclear Research Center, Atomic Energy Authority, Cairo, Egypt. 2.—e-mail: adelhashhash@gmail.com. 3.—e-mail: ee175sh@yahoo.com

Nano-crystalline samples of cerium substituted cobalt ferrites with chemical formula $CoCe_xFe_{2-x}O_4$ ($0.0 \le x \le 0.1$) were prepared using the citrate auto-combustion method. The prepared ferrites were characterized by x-ray diffraction (XRD), Fourier transform infrared spectroscopy spectra (FTIR), transmission electron microscopy (TEM), and a vibrating sample magnetometer (VSM). The XRD patterns and FTIR spectra confirm that the prepared samples reveal the formation of a single-phase spinel structure. TEM micrographs showed that the particles are made up of spherical and elongated nano-metric shapes. A limitation of the size of nanoparticles is observed as the Ce^{3+} concentration increases. VSM measurements showed that the coercivity H_c and magnetization values M_s are strongly dependent on Ce^{3+} content and particle size. The values of H_c lie in the range of (411–1600 G), which suggest that these samples are convenient for different applications. The alternating current electrical conductivity (σ), dielectric permittivities (ε', ε''), and dielectric loss tangent (tan δ) were studied at different ranges of frequency and temperature. The relation of conductivity with temperature revealed a semiconductor to semi-metallic behavior as cerium concentration increases. The variation in (tan δ) with frequency at different temperature shows abnormal behavior with more than one relaxation peak. The conduction mechanism used in the present study has been discussed in the light of cation–anion–cation interactions over the octahedral B-site.

Key words: CoCe–ferrite, XRD, spherical nanomaterials, AC conductivity

INTRODUCTION

Crystalline magnetic materials formed at the nanoscale have attracted several scientists due to their novel properties, which are significantly different from those of their bulk counterparts.[1] Currently, considerable interest in nano-crystalline oxide materials exists owing to their unusual properties. Decreasing particle size results in some remarkable phenomena. Unusual electric and magnetic properties in these materials takes place due to a great interest in their potential applications in many technologically important area such as gas sensing, electronics semiconductors, electrical characteristics, medicine magnetic drug delivery and magnetic applications.[2,3]

Cobalt ferrite belongs to the class of hard magnetic materials. Hard materials exhibit large coercivity (H_c) and magnetization, high resistivity, good chemical stability, and are regarded as an ideal candidate for several technological applications.[4] It is interesting that the structure, electrical and magnetic properties of spinel ferrites like $CoFe_2O_4$, can be modified by varying the type and amount of substitute into the spinel lattice. By substitution of rare earth ions (RE) like cerium in place of iron Fe^{3+} in the spinel ferrites, the (RE^{3+}-Fe^{3+}) interactions appear, and result in 3d–4f coupling.[5,6] This coupling leads to an enhancement in the magnetic and electric properties due to the orbital shape of the unpaired (4f) electrons of RE, which produces a magnetic anisotropy. In general,

(Received July 27, 2015; accepted October 5, 2015; published online October 28, 2015)

the electronic configuration, ionic radius, and electrostatic potential are the most important factors affecting the behavior of ferrites.[7]

In this connection, the effects of cerium substitution on the properties of spinel ferrites have been reported by few researchers. Khandekar et al.[8] studied the effects of Ce^{3+} doping on the structural, morphological, and gas sensing properties of the $CoFe_2O_4$. They reported that the addition of Ce (4 wt.%) has a strong influence on the response and operating temperature of the sensor materials and thus can serve as acetone-sensing sensors. The structure and direct current (DC) electrical resistivity of $CuFe_{2-x}Ce_xO_4$ ferrites with ($0.0 \le x \le 0.8$) was measured at different temperatures by Malana et al.[9] They found that the lattice constant increases up to $x = 0.4$ due to larger ionic size of cerium and then decreases due to lower solubility of cerium as compared to that of iron. The DC electrical resistivity increases with an increase in dopant concentration while it decreases with rise in temperature exhibiting semiconductor behaviour. The dielectric constant and dielectric loss tangent decrease with exponentially increases in frequency reflecting normal dielectric behavior of ferrites.

Nanocrystalline samples of Ce^{3+} substituted Co-Cr ferrite with chemical formula $CoCr_{0.04}Ce_xFe_{1.96-x}O_4$ ($0.0 \le x \le 0.1$) has been synthesized by the co-precipitation method.[10] They reported that the saturation magnetization decreased with increasing Ce^{3+} content, while the coercivity is related to the microstructure of Ce^{3+} substituted samples. The obtained results suggest that the investigated materials are suitable for different applications.

Recently, several methods have been employed to synthesize highly crystalline and uniformly sized magnetic nanoparticles of ferrites. The citrate autocombustion method has gained much importance, while it offers many advantages such as temperature processing, better homogeneity for the synthesis materials, and formation of the nanosized particles of ferrite powders.[10] In the present work we report the synthesis and characterization of nanoferrites $CoFe_{2-x}Ce_xO_4$ prepared by the citrate autocombustion method. To the best of our knowledge, no detailed studies have been reported in the literature on the structure, electric, and magnetic properties for these materials.

EXPERIMENTAL

Preparation of Samples

Nanocrystalline $CoCe_xFe_{2-x}O_4$ ($x = 0.0$, 0.01, 0.03, 0.05, 0.07, 0.1) was prepared using the citrate auto-combustion method.[11,12] The chemical reagent grade $Co(NO_3)_2{\cdot}6H_2O$, $Ce(NO_3)_3{\cdot}6H_2O$, $Fe(NO_3)_3{\cdot}6H_2O$ and citric acid ($C_6H_6O_7$) were used as starting materials. The metal compound and citric acid were dissolved in minimum amounts of doubly distilled water. The citric to the all-metal molar ratio was chosen as 1:1. Metal solutions were mixed together and then the citric solution was added, followed by 2-h stirring and heating (80°C) using a hot magnetic stirrer. Ammonia solution (NH_4OH) was then added drop by drop to adjust the PH value at 7–8; then the solution turned darker and more viscous. Heating was initialized on a hot plate to evaporate the water until a dry viscous gel formed at about 200°C. Finally, the burned gel was converted into fluffy powder, which was collected and ground in an agate mortar to obtain a fine powder.

Measurements

X-ray diffraction (XRD) patterns of the samples are obtained at room temperature using a Philips diffractometer (expert MPD) with CuKα radiation (λ = 1.5418 Å). The structure parameters of the samples; lattice constant (a), grain size (D), x-ray density($\rho_{\text{x-ray}}$), bulk density (ρ_{bulk}), and porosity (P) can be calculated using the following relations[13,14]:

$$a = d\sqrt{(h^2 + k^2 + l^2)}, \tag{1}$$

$$D = \frac{0.89\lambda}{B_{1/2}\cos\theta}, \tag{2}$$

$$\rho_{\text{bulk}} = \frac{m}{\pi r^2 h}, \tag{3}$$

$$\rho_{\text{x-ray}} = \frac{8M}{N_A a^3}, \tag{4}$$

$$P = 1 - \frac{\rho_{\text{bulk}}}{\rho_{\text{x-ray}}}, \tag{5}$$

where d is the interplanar distance and (hkl) are Miller indices of the crystal planes. λ is the x-ray wavelength, θ is the Bragg's diffraction angle, and $B_{1/2}$ is the full width at half maximum (FWHM). The symbols (m, r, h) are, respectively; the mass, radius, and thickness of the sintered ferrite samples pressed in a form of a pellet. M is the molecular weight and N_A is the Avogadro's number. The energy dispersive x-ray spectrometer (EDX) model (JFC-1500 JEOL) used for determining the elemental composition by energy dispersive peaks of the samples. The shape and grain size of the prepared nano-ferrite samples were observed by high-resolution transmission electron microscope (HR-TEM) images (PHILIPS CM-200 model). Fourier transform-infrared (FT-IR) spectra were recorded at room temperature in the frequency range of 4000–250 cm^{-1}, employing KBr disc technique and using a (Jasco FT-IR 310) spectrophotometer. The magnetic measurements were recorded using a vibrating sample magnetometer (VSM 9600-1 LDJ, USA) at room temperature with a maximum applied external magnetic field up to 6 kO_e. The electrical measurements were carried out on the samples in the form of a disc with polished surfaces covered by silver paste. The dimensions of the samples were (~10 mm in diameter and ~4 mm in thickness). A SR830 DSP Lock-in amplifier is used

to measure the voltage difference (V_R) between the two ends of known resistance R, which is connected in series with the sample (in an equivalent RC circuit). Measurements were carried out at frequency range (10^2–10^5 Hz) in a vacuum atmosphere of about 1.3×10^{-3} Pa. Data logger software is used for controlling and collecting the data through IEEE-488 GPIB and 332 serial interfaces with the different equipment.

RESULTS AND DISCUSSION

Structural Analysis

XRD patterns for the general formula $CoCe_xFe_{2-x}O_4$ (x = 0.0, 0.01, 0.03, 0.05, 0.07, 0.1) ferrite system are shown in Fig. 1. X-ray characterization shows that all samples exhibit a single phase cubic spinel structure. The broadening of the diffraction peaks indicated the nanometric nature of the prepared samples. The effect of Ce^{3+} substitution on the lattice parameter (a) and grain size (D) is shown in Fig. 2. It is observed that the lattice constant increases up to x = 0.05 and thereafter it decreases. The replacement of the smaller Fe^{3+} (0.65 Å) ions by the larger Ce^{3+} (1.14 Å) ions[8] increases the lattice constant due to the expansion of the unit cell. The decrease in lattice constant with further addition of Ce^{3+} ($x \geq 0.07$) can be interpreted based on the site preference of Ce^{3+} in the octahedral B-site, preparation condition, and lower solubility of Ce^{3+} compared to Fe^{3+}.[9] In spinel structure, the presence of Ce^{3+} in the centre of the cube causes distortion in octahedral and tetrahedral symmetry, which affects the lattice constant, bond lengths, and central frequency band.[15] It can be seen from Fig. 2 that the grain size decreases with increasing Ce^{3+} content. This behavior can be explained as a result of growing the concentration of Ce^{3+} ions, which occupy the grain boundaries and causes limitation of the grain size.[16] This result is also observed in Fig. 1 as the broadening of the XRD peaks increases by further addition of Ce^{3+}. Khandekar et al.[8] investigated the structure properties of Ce-doped $CoFe_2O_4$ ferrites, but they might not have succeeded in obtaining a single-phase spinel structure for the as-prepared sample with Ce^{3+} concentration x = 0.08. This sample reported a grain size of (D = 25 nm), which is large compared to the grain size (D = 20 nm) for our sample at x = 0.1.

Figure 3a illustrates the variation of x-ray density $\rho_{x\text{-ray}}$ and porosity (P) with Ce^{3+} content. It is clear that the $\rho_{x\text{-ray}}$ exhibits a reverse trend compared to that of the porosity. The increase in $\rho_{x\text{-ray}}$ with Ce^{3+} content is interpreted to be due to that the molar mass of the Ce^{3+} atom (140 g/mol), is greater than that of the Fe^{3+} atom (55.8 g/mol). Figure 3b shows the variation of the bulk density ρ_{bulk} and porosity (P) with Ce^{3+} concentration. It is observed that the values of ρ_{bulk} calculated by the mass to volume ratio, lies in the range (1.63–1.82 g/cm^3), which are found to be smaller than the values of $\rho_{x\text{-ray}}$ (5.34–5.51 g/cm^3).

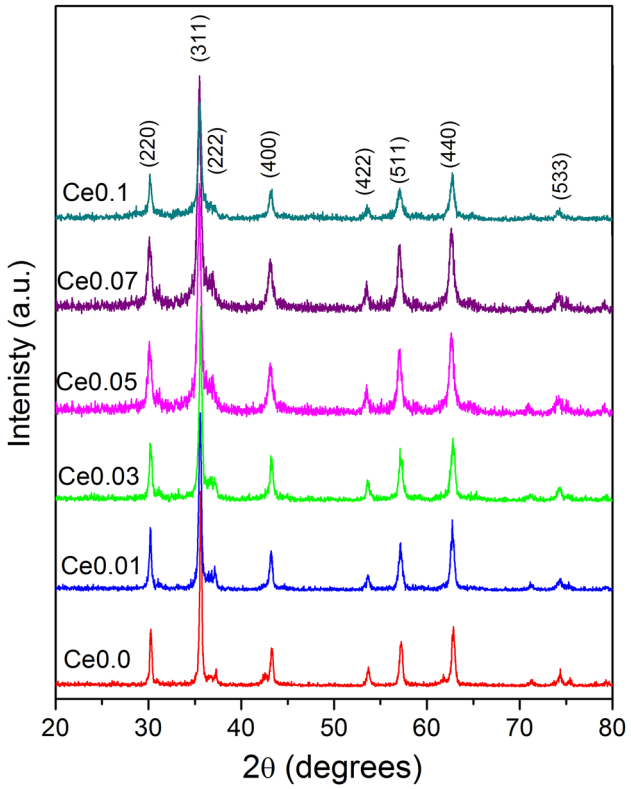

Fig. 1. X-ray diffraction patterns of $CoCe_xFe_{2-x}O_4$.

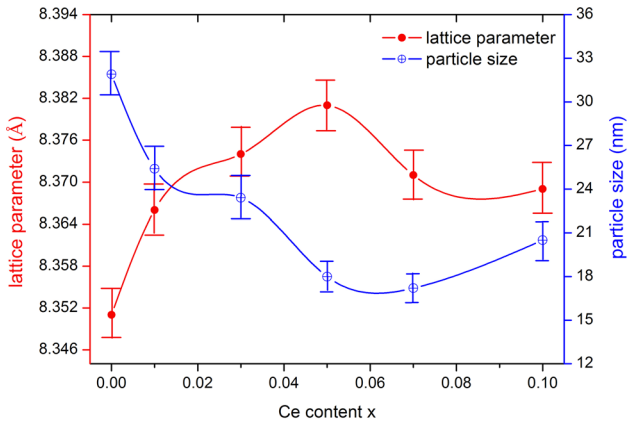

Fig. 2. The variation of lattice parameter and particle size with cerium content x.

This behavior can be attributed due to the existence of pores, which were formed and developed during sample preparation and the sintering process.[10] The porosity P changes in the range (67–69%) due to the substitution of Ce^{3+} as shown in Fig. 3. The high value of P represents the special porous of ceramics materials. Table I shows a comparison between the method of preparation, structure parameters, and magnetic properties for the samples; $CoCe_xFe_{2-x}O_4$ with (x = 0.0, 0.1) and previous studied samples; $CoFe_2O_4$[8] and $CoCr_{0.04}Ce_{0.1}Fe_{1.86}O_4$.[10] It is clear that the values of the lattice constant a, grain size D, and

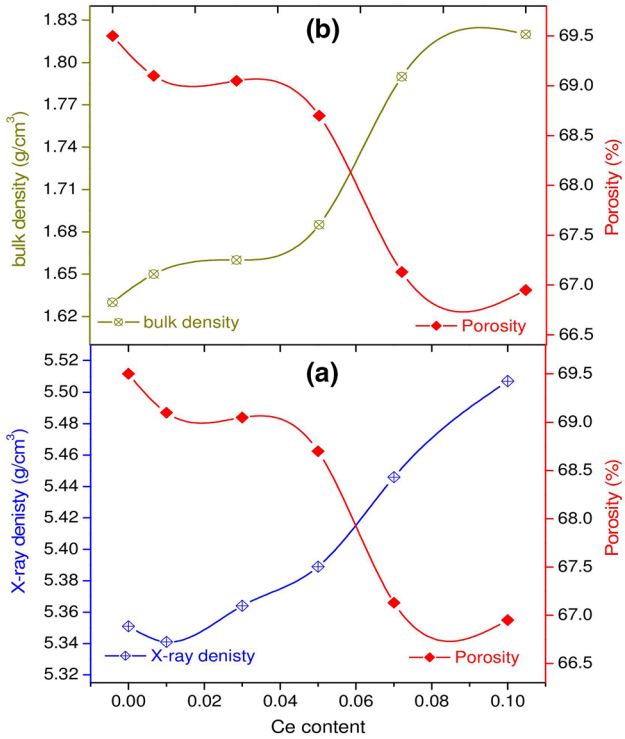

Fig. 3. (a, b) The relation of: (a)—x-ray density (b)—bulk density and porosity with cerium concentration.

porosity P depends mainly on the preparation condition.

Morphology and Elemental Analysis

The (HR-TEM) micrographs for the three prepared samples $CoCe_{0.1}Fe_{1.9}O_4$, $CoCe_{0.05}Fe_{1.95}O_4$, and $CoCe_{0.01}Fe_{1.99}O_4$ are shown in Fig. 4a, b, and c respectively. The majority of the particles have a spherical shape, while some particles are elongated in the form of a rectangular shape.[17] Some agglomeration is also observed in the (HR-TEM) micrographs, which may due to the interaction force between the magnetic particles. This interaction produces a low surface energy state and reduces the interfaces between the nanoparticles.[18] Figure 4d shows an example of the shape of the fluffy final product for the as-prepared sample. The EDX spectrum for the sample $CoCe_{0.1}Fe_{1.9}O_4$, indicated the presence of iron, cobalt, cerium and oxygen elements as shown in Fig. 5a. The extra peak for Cu is attributed to the sample grid.[19] The EDX analysis reveals that the atomic ratio of the metals (Fe^{3+}, Co^{2+}, Ce^{3+}) is near the stoichiometric values. The presence of bright spots forming rings pattern in Fig. 5b is an indication of the crystalline nature of the spinel ferrite samples.[17]

Infrared Spectra

Figure 6 shows FT-IR spectra recorded at room temperature in the frequency range 250–4000 cm^{-1} for the $CoCe_xFe_{2-x}O_4$ ferrite system. The vibration frequencies of the samples are given in Table II. The common feature of the ferrite materials is the existence of two main infrared absorption bands below 1000 cm^{-1}.[20] These two bands are confirming the formation of a single phase spinel structure. The high frequency band υ_A in the range 569–577 cm^{-1} is related to the vibration of the tetrahedral metal oxygen bond (M–O), which is characteristic of the tetrahedral A-site. The low frequency band υ_B lies in the range 372–381 cm^{-1} and is assigned to the bending vibrations of the (M–O) bonds in the octahedral complexes. The differences in vibration frequencies; υ_A and υ_B between the two crystallographic A and B-sites, can be attributed to the change in bond length (M–O), where the ionic radius of A-site is smaller than B-site.[3]

The observed two broad bands at 1619 cm^{-1} and 3450 cm^{-1} are due to the stretching vibration in the residual H-O-H modes of water molecules. Residual water and hydroxy group were always detected in the prepared ferrite samples doped with cerium.[21] The sharp bands detected at 1358 cm^{-1} are attributed to the symmetric stretching of the carboxyl group (COOH). The bands at 1113 cm^{-1} are assigned to asymmetric stretching vibration of the adsorbed NO_3 produced as a residue from the nitrate group after the combustion of the samples.[12]

Magnetic Properties

Magnetic hysteresis M-H of $CoCe_xFe_{2-x}O_4$ ($0.0 \le x \le 0.1$) nanoparticles measured at room temperature using VSM represented in Fig. 7. The magnetic parameters; saturation magnetization (M_s), coercivity (H_c), and remanent magnetization (M_r) obtained from the M–H curves are summarized in Table II. The relationship between saturation magnetization and coercivity versus the substituted amount x are illustrated in Fig. 8. The saturation magnetization increases with cerium content up to $x = 0.01$ showing a maximum value, and thereafter it decreases. In the present nanocrystalline samples, Co^{2+} and Ce^{3+} ions have a favorable fit of charge distribution in the crystal field of the octahedral sublattice, whereas Fe^{3+} ions are distributed between A and B-sites.[8,10] At $x = 0.01$, the initial increase in M_s may be due to the presence of Co^{2+} (3 μ_B) and Fe^{3+} (5 μ_B) ions in the octahedral B-site. So as the net magnetic moment is increased, thus M_s increases. As the introduction of Ce^{3+} ions (2.5 μ_B) progress in the present unit cell, the RE^{3+}–Fe^{3+} interaction appears through the 3d–4f electron coupling, which decreases the A–B exchange interactions strength and consequently decreases the saturation magnetization.[6,22] The correlation between M_s and the particle size D is also clear, while D decreases with the compositional parameter x due to the low solubility of Ce^{3+}. As a result, Ce^{3+} is substituted in the grain boundary and reduces the growth in the size of nanoparticles.[16] This in turns

Table I. Comparison between the preparation methods, structure properties; (lattice parameter a, grain size D, porosity P) and magnetic parameters; (saturation magnetization M_s, coercivity H_c) for the represented samples

Samples	Preparation method	a (Å)	D (nm)	P (%)	M_s (emu/g)	H_c (G)
$CoFe_2O_4$ (our sample)	Citrate autocombustion	8.351	31.9	69.5	–	–
$CoFe_2O_4$[8]	Molten-salt (M-S)	8.358	28	–	–	–
$CoCe_{0.1}Fe_{1.9}O_4$ (our sample)	Citrate autocombustion	8.369	20	67.0	19.0	411
$CoCe_{0.1}Cr_{0.04}Fe_{1.86}O_4$[10]	Coprecipitation	8.387	72.9	38.0	15.3	773

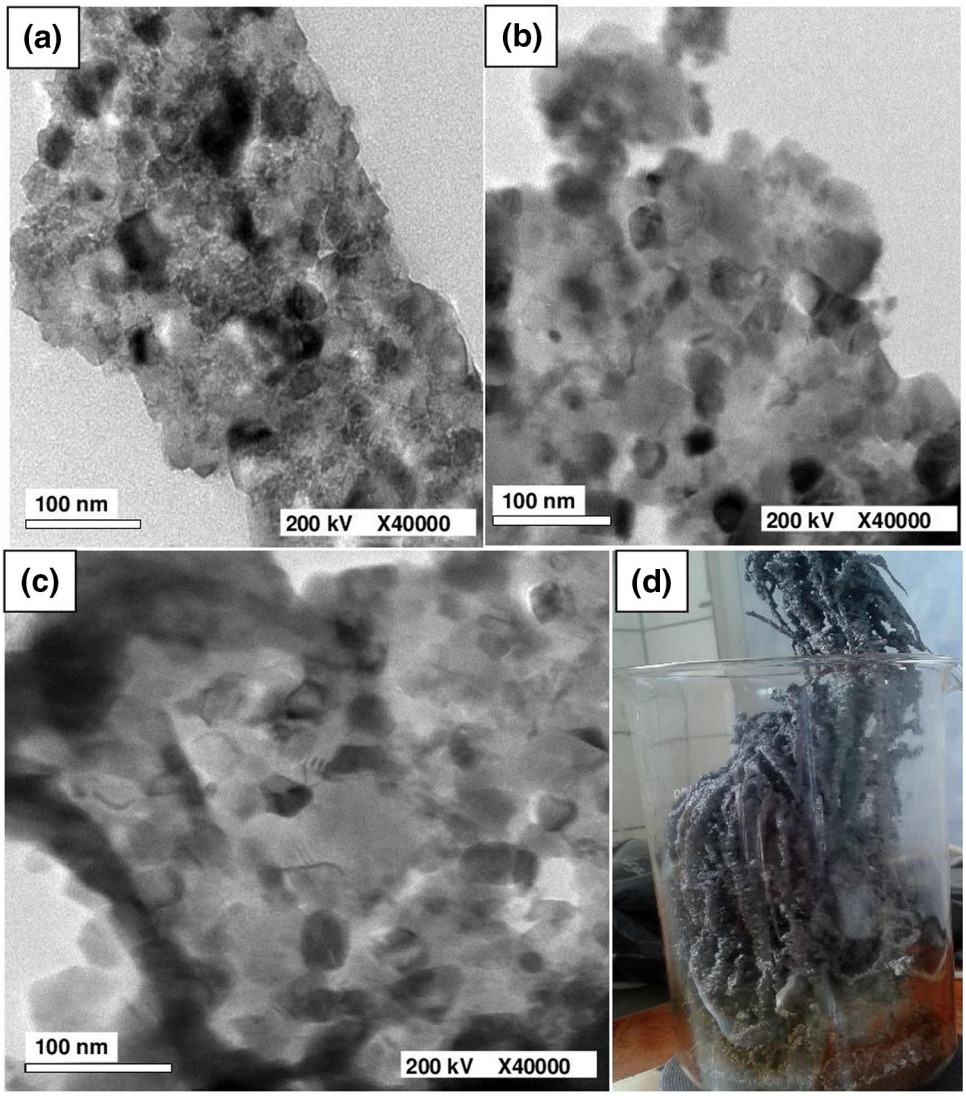

Fig. 4. (a–c) HR-TEM Micrographs of the samples with ($x = 0.1, 0.05, 0.01$) respectively and (d) The shape of the fluffy final product for the prepared samples.

enhances the presence of single domain nanoparticles and reduces the values of M_s. Depending on the values of M_s and the molecular weight M of each sample, the magnetic moment (n_B) in the Bohr magneton (μ_B) can be calculated using the relation[23]: $n_B = \frac{M \times M_S}{5585}$. It is clear that the values of the magnetic moment (n_B) decrease with x Table II, in a behavior similar to the saturation magnetization (M_s) and grain size (D).

Magnetization studies showed that the coercivity H_c give an initial increase for the sample with $x = 0.01$, then it gradually decreases with increasing cerium concentration Fig. 8. Two different mechanisms cause a variation in H_c values: Firstly,

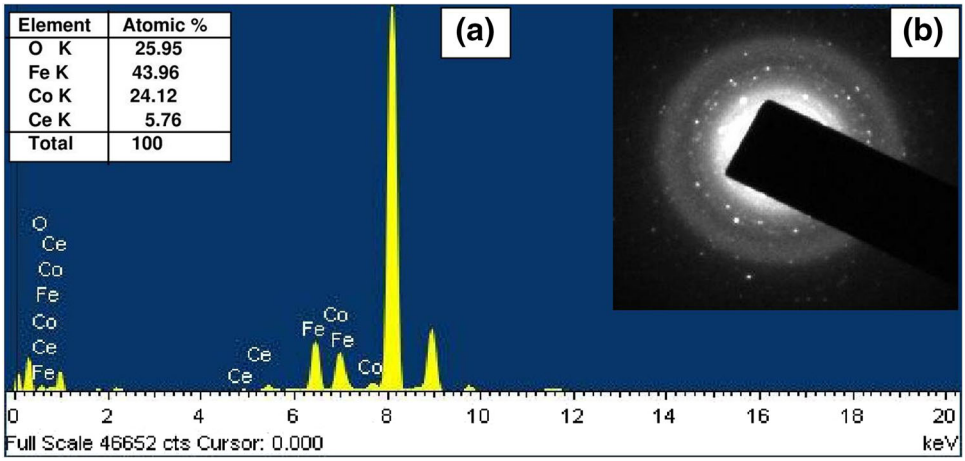

Fig. 5. (a) EDX patterns and (b) electron diffraction patterns for the $CoCe_{0.1}Fe_{1.9}O_4$ sample.

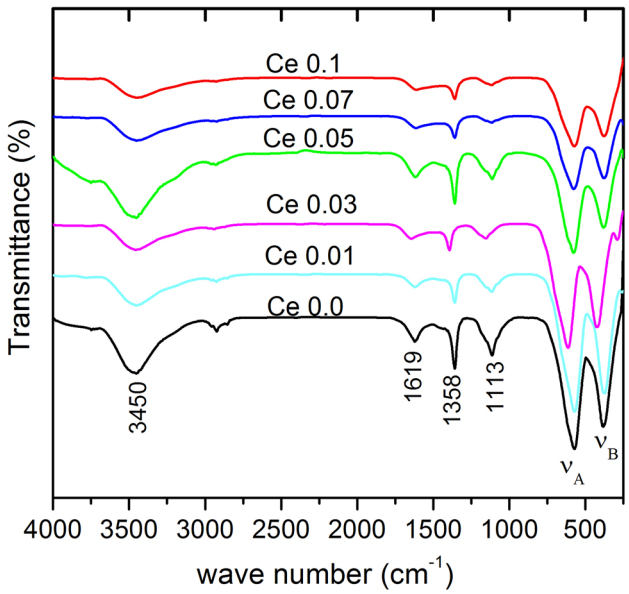

Fig. 6. FT-IR absorption spectra of $CoCe_xFe_{2-x}O_4$.

the coercive field is influenced by a property known as magnetic anisotropy.[15,24] This represents the force required to rotate the magnetization vector as a magnet out of its equilibrium direction. Low anisotropy results in a low H_c. In the present samples the addition of cerium decreases the anisotropy field, which in turns decreases the domain wall energy and H_c starts to decrease.[24,25] Secondly, there is a relationship between the coercive field and grain size. In the nanoferrite system $CoCe_xFe_{2-x}O_4$, the formation of single domain and movement of the domain walls could also create a variation in coercivity. The values of H_c (as seen in Table II) lie in the range of (411–1600G), which suggest that these samples are convenient for different applications. A sample with (H_c = 411 G) is convenient for sensing, switching, and high frequency applications, while the samples in the range ($600 < H_c < 1000$ G) are suitable for longitudinal magnetic recording media. Furthermore, samples with ($H_c > 1000$ G) are suitable for transverse magnetic recording media.[10,15] It can be noticed that the value of M_s for the sample ($x = 0.1$) is higher than its value for the previously studied sample $CoCr_{0.04}Ce_{0.1}Fe_{1.86}O_4$[10] Table I, which can be interpreted as due to the replacement of the larger ionic magnetic moment (Fe^{3+}, 5 μ_B) with a smaller ionic magnetic moment (Cr^{3+}, 3 μ_B). Table I also shows correlation relation between the H_c and D values for these two samples.

Electric Properties

Temperature and Frequency Dependence of Conductivity

Figure 9 illustrates typical curves correlating the conductivity as ($\ln \sigma$) with the reciprocal of temperature as ($1000/T$) at different frequencies for the $CoCe_xFe_{2-x}O_4$ system with ($0.0 \le x \le 0.1$). For the samples with low concentration of Ce^{3+} ($0.01 \le x \le 0.03$), the conductivity increases with increasing temperature, where the semiconducting behavior becomes more predominant. This behavior of the conductivity can be divided into two main regions; the first region is highly frequency dependent whereas the second region is frequency independent. In the low temperature region, the thermal energy is not enough to liberate charge carriers and increasing the frequency enhances their hopping. In the high temperature region, the conductivity becomes frequency independent where all the curves are merged together indicating the formation of a disordered state. As Ce^{3+} concentration increases in this compound ($0.05 \le x \le 0.1$), semiconductor to semi-metallic transition occurs at low temperature where the conductivity becomes frequency independent.

Goodenough[26] pointed out that in the spinel ferrites both the cation–anion–cation interactions and the

Table II. FT-IR vibration frequencies (ν_A, ν_B) and magnetic properties (M_s, H_c, M_r, n_B) of $CoCe_xFe_{2-x}O_4$ nanoferrite samples

x	High band frequency ν_A (cm^{-1})	Low band frequency ν_B (cm^{-1})	Saturation magnetization M_S (emu/g)	Coercivity H_c (G)	Remanent magnetization M_r (emu/g)	Magnetic moment n_B (μ_B)
0.0	572	381	32.9	972	17.3	1.38
0.01	571	372	38.2	1573	19.0	1.61
0.03	569	372	27.5	1603	13.6	1.17
0.05	577	380	21.5	1342	9.0	0.92
0.07	576	380	21.9	1364	8.6	0.94
0.1	574	380	19.0	411	6.7	0.83

cation-cation interactions can be simultaneously present in the structure. Studies on different spinel ferrite[27,28] have shown that for transition metal ions with $5 \le m \le 8$ (where m is the number of electrons in d levels) as in CoO the cation–anion–cation interaction must be stronger. In the case of strong cation–anion–cation interactions and weak cation–cation interactions, the materials have semiconductor (or insulator) behavior. This means that there are two transition elements with open 3d shells, Co^{2+} ($3d^7$) and Fe^{3+}($3d^6$), which leads to two types of cation–anion–cation interactions designated as [Fe^{3+}-O^{2-}-Fe^{3+}] and [Co^{2+}-O^{2-}-Co^{2+}] over the octahedral B-site. Substitution of Ce^{3+} ions in place of Fe^{3+} ions affects the [Fe^{3+}-O^{2-}-Fe^{3+}] and [Co^{2+}-O^{2-}-Co^{2+}] interactions. As the substitution of cerium progressed in the present unit cell, the cation–anion-cation interaction becomes less predominant. This leads to the transition from semiconductor to semi-metallic behavior in this system as illustrated in Fig. 9. Sattar et al.[29] reported that RE ions occupy either the Fe^{3+} position or go to the grain boundaries. They have excluded the probability that the RE occupy the A-site in place of Fe^{3+} ions. This is due to the fact that the A-sites are too small to be occupied by the RE with large ionic radius, i.e., Ce^{3+} [r_{Ce} = 1.14 Å]. The presence of RE ions at the B-site will decreases the hopping of the charge carriers and, hence, the electrical conductivity.

The Dielectric Properties

The variation of the dielectric constants (ε', ε'') as a function of temperature for the nanoferrite samples at different frequencies is shown in Figs. 10 and 11. The relations represent a sensitive dependence of ε' and ε'' on both frequency and temperature as a function of the compositional parameter x. From the figures, it can be seen that the general trend is the increase in ε' and ε'' with increasing temperature, and the relaxation process takes place at nearly the same frequency. The increase in the dielectric constant takes place with different rates depending on Ce^{3+} content. At low temperature the relations show continued increase in ε' and ε'' with temperature until reaching a maximum for the samples with Ce^{3+} concentration (x = 0.0 and 0.01). It is worth noticing that, the amplitude of this peak decreases as the frequency increases. At ($x \ge 0.03$), the relaxation peaks disappeared, and the relation shows a normal behavior, where ε' and ε'' increase with increasing temperature. The occurrence of a

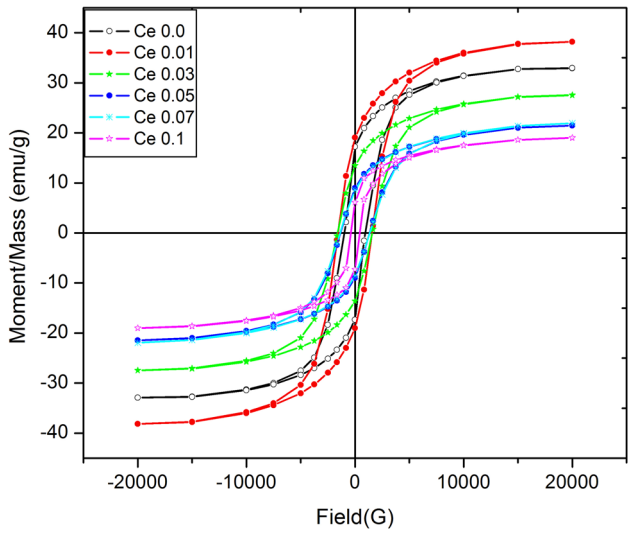

Fig. 7. Magnetic hysteresis loop of $CoCe_xFe_{2-x}O_4$ ferrite nanoparticles.

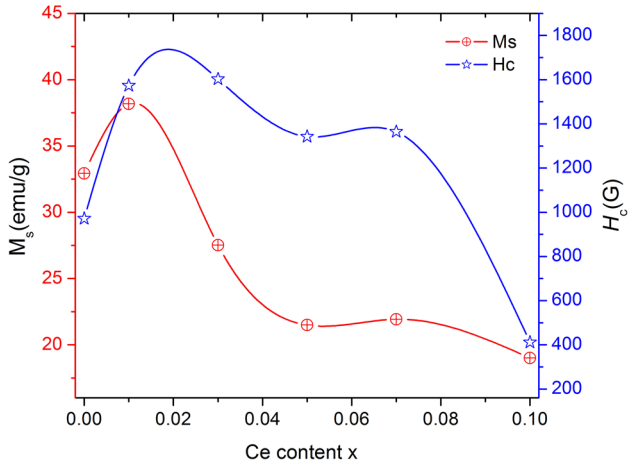

Fig. 8. Dependence of magnetization (M_s) and coercivity (H_c) on Ce^{3+} concentration.

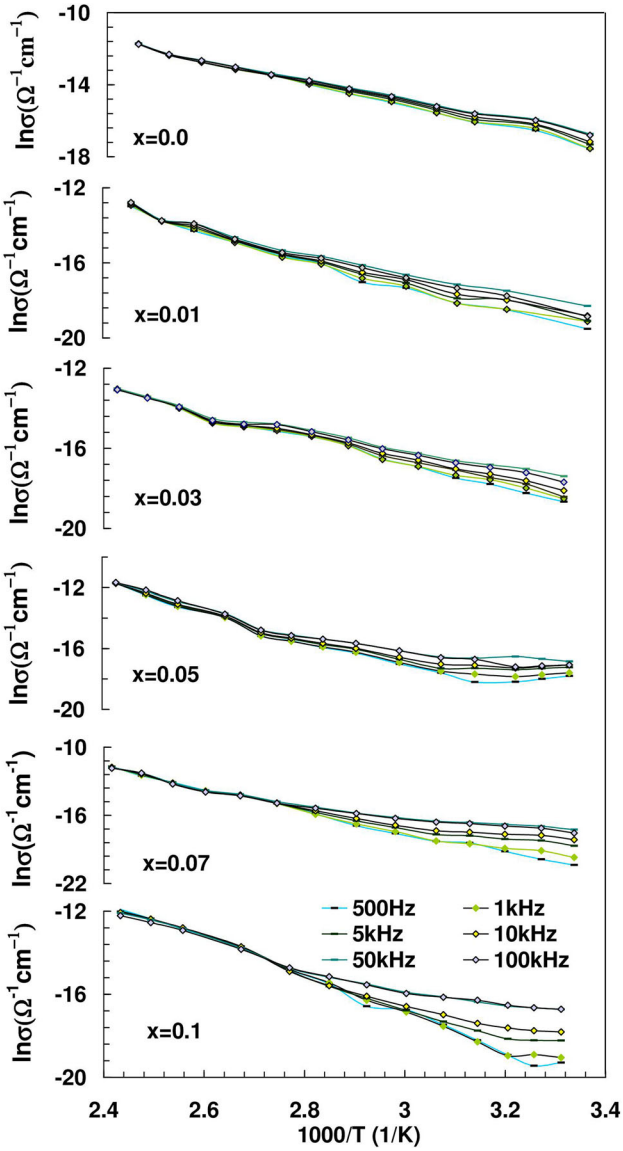

Fig. 9. Conductivity as ln (σ) versus 1000/T for $CoCe_xFe_{2-x}O_4$ at different frequencies.

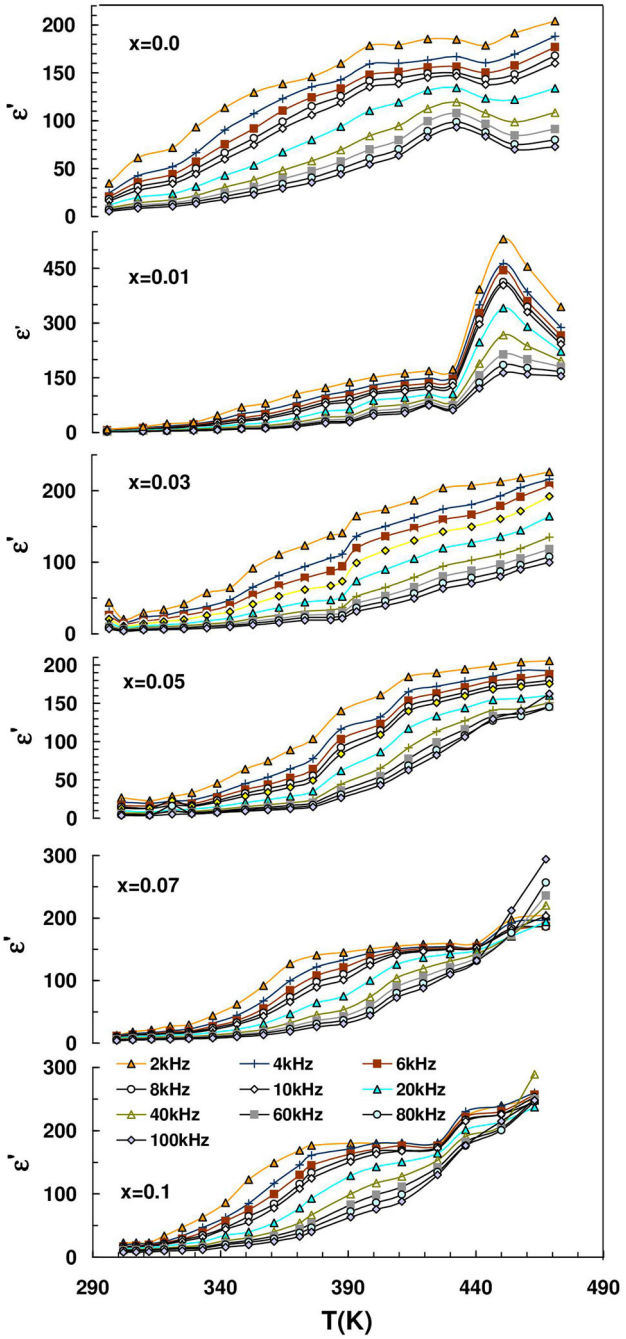

Fig. 10. Temperature dependence of ε' at different frequencies of $CoCe_xFe_{2-x}O_4$.

peak at a certain range of frequencies can be attributed to the natural oscillation frequency of the dielectric dipoles matching the thermal energy.[30] This type of behavior was observed in a number of ferrites.[31,32] At relatively low temperature, the thermal energy for the sample is not sufficient to free the localized dipoles to be oriented in the field direction; therefore, the process has a weak contribution to the polarization and the dielectric constant.[33] As the temperature increases, the dipoles get enough thermal energy to be able to obey the change in the external field more easily. This in turn enhances their contribution to the polarization leading to an increase of the dielectric constant.

Figure 12 illustrates the variation of the loss tangent (tan δ) with frequency for the investigated samples. The relaxation spectra with more than one relaxation peak are observed at low and intermediate frequencies for the samples with concentration x = 0.0 and 0.01. Also the intensity of the loss peak increases with increasing temperature and becomes broader. By further increase in cerium concentration ($0.03 \leq x \leq 0.1$), only one relaxation peak is observed. This peak appears when the hopping frequency of charge carriers is in resonance with the frequency of the applied electric field. As a result, maximum electric energy is transferred to the electrons, and the loss shoots up at resonance.[34] The decrease of (tan δ) with increasing frequency is

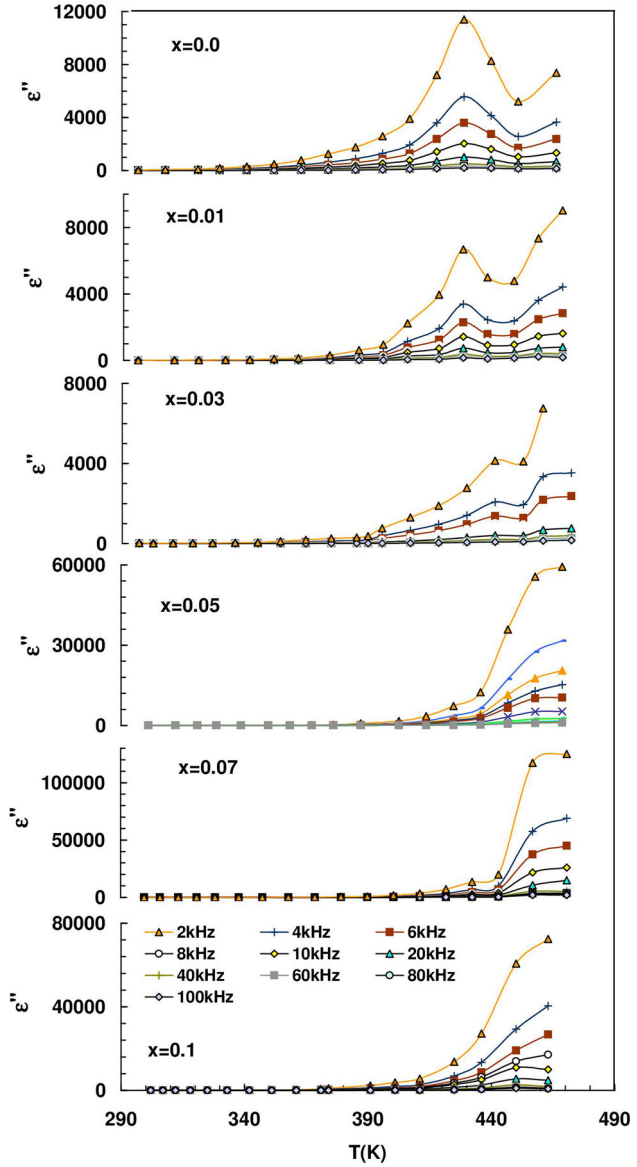

Fig. 11. Temperature dependence of ε'' at different frequencies of $CoCe_xFe_{2-x}O_4$.

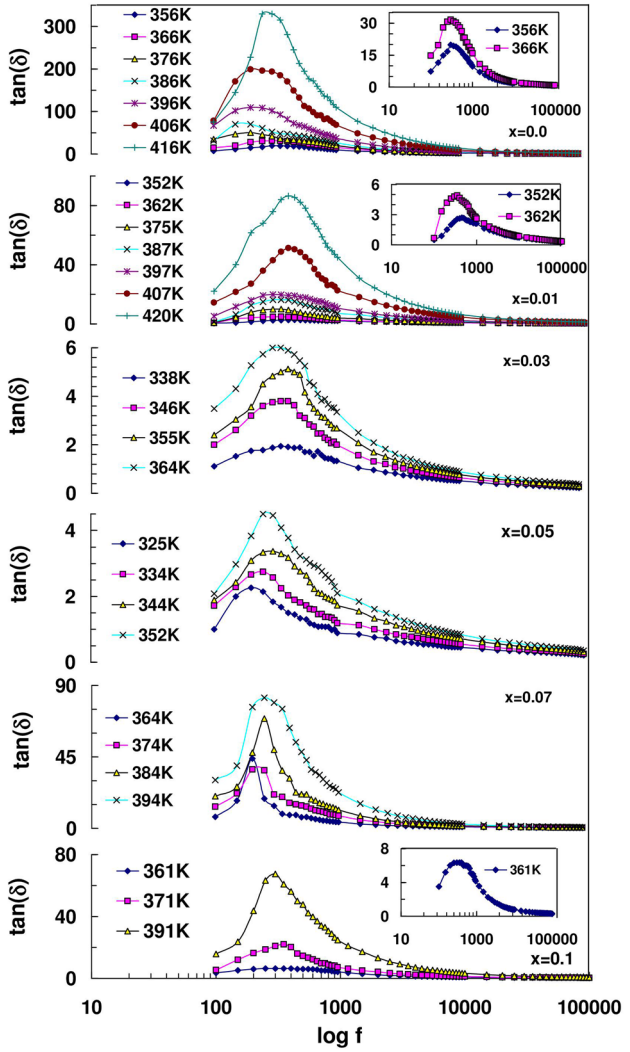

Fig. 12. Tan δ versus frequency (log f) of $CoCe_xFe_{2-x}O_4$ at different temperature.

attributed to the fact that the hopping frequency of charge carriers cannot follow the changes of the externally applied electric field beyond a certain frequency limit.[35] The dielectric loss tangent (tan δ) in these compounds can be written as a function of the relaxation time τ and the frequency f:

$$\tan(\delta) = F(f, \tau),$$

where the change in temperature affects the relaxation time as:

$$\tau = \tau_o \exp(-E/k_B T).$$

E is the activation energy of the relaxation process and k_B is the Boltzmann's constant. The relaxation time τ is calculated from the relation between tan (δ) and frequency (Fig. 12).

The condition for observing a maximum in dielectric losses of dielectric material is given by $\omega\tau = 1$, where $\omega = 2\pi f_{max}$. A plot of $\ln\tau$ versus reciprocal of temperature for the ferrite system $CoCe_xFe_{2-x}O_4$ gives straight lines as shown in Fig. 13. From this relation two relaxation processes are present in the samples with $x = 0.0$ and 0.01, but for the samples with ($x \geq 0.03$) only one relaxation process exists. In the present composition under investigation Co^{2+} and Ce^{3+} ions in the unit cell are occupying the octahedral B-site as reported earlier.[4,29] The introduction of Ce^{3+} in place of Fe^{3+} in present unit cell affects the hopping conduction mechanism between [Fe^{3+}-O^{2-}-Fe^{3+}] and [Co^{2+}-O^{2-}-Co^{2+}] over the octahedral B-site, which are responsible for the electric conduction and dielectric polarization. The activation energies are calculated from the slope of the observed linear relations for these

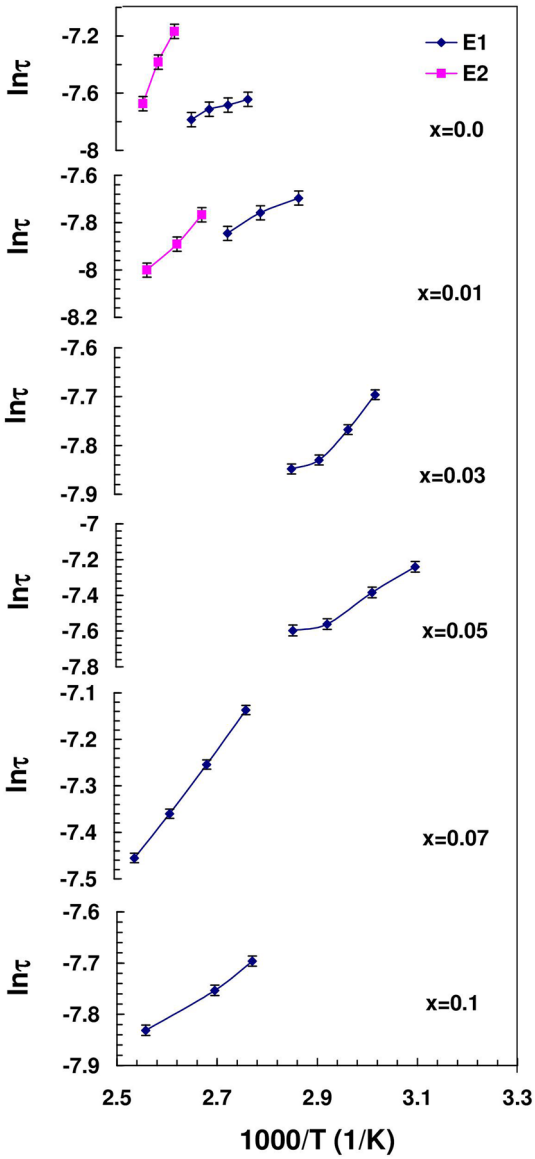

Fig. 13. Relaxation time ln τ versus 1000/T of $CoCe_xFe_{2-x}O_4$ nanoferrite.

Table III. The activation energy obtained from the relation of ln τ versus 1000/T shown in Fig. 13

Ce content (x)	ΔE_1(ev)	ΔE_2(ev)
0.0	0.053(6)	0.358(7)
0.01	0.071(6)	0.144(9)
0.03	0.063(1)	–
0.05	0.136(3)	–
0.07	0.131(3)	–
0.1	0.054(1)	–

processes and are listed in Table III. The small values of the activation energy in the low temperature region confirm the electronic character of the conduction process, which consists of electron hopping between the ions of different valences. Similar behavior was observed by El-sayed.[36,37]

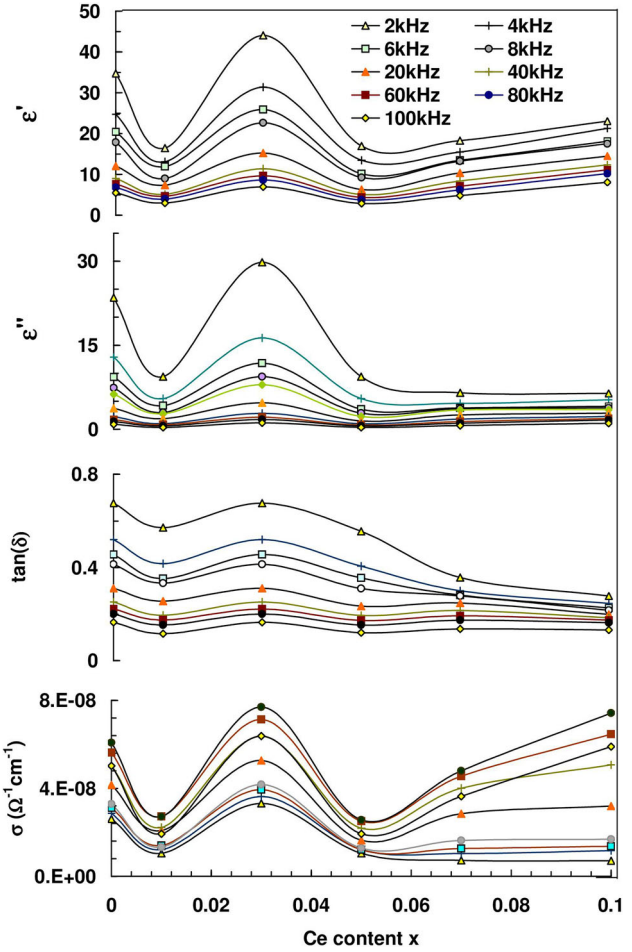

Fig. 14. Room temperature dependence of (ε'), (ε''), tan (δ) and (σ) on Ce^{3+} content (x) at different frequencies for $CoCe_xFe_{2-x}O_4$ nanoferrite.

Figure 14 shows the compositional dependence of (ε', ε'', tan (δ) and σ) with different frequencies at room temperature for $CoCe_xFe_{2-x}O_4$. As shown from the figure, (ε', ε'' and tan (δ)) have the same trend as the conductivity, which confirms the assumption that the mechanisms of the conductivity and dielectric are of the same origin. It is clear that the values of (ε', ε'', tan (δ) and σ) decreased at initial Ce content (x = 0.01). As Ce ions substitution increases, the values of (ε', ε'', tan (δ) and σ) start to increase up to critical concentration x = 0.03 and thereafter start to decrease. This result may be attributed due to the hopping conduction mechanism, i.e., the hopping conduction mechanism between [Fe^{3+}-O^{2-}-Fe^{3+}] and [Co^{2+}-O^{2-}-Co^{2+}] over the octahedral B-site. In other words, as Ce content increases, the cation–anion–cation interactions are expected to be less predominant due to the presence of RE ions at the B-site.[29]

CONCLUSION

Nanoparticles of spinel ferrites $CoCe_xFe_{2-x}O_4$ with ($0.0 \le x \le 0.1$) were synthesized in single phase by the citrate auto-combustion method. The transmission electron microscopy (TEM) micrographs of the synthesized ferrites showed that the particles formed in spherical and elongated shapes with grain size in the range of 16–31 nm. The magnetic parameters (M_s, H_c) decrease with increasing doping percent of cerium. This behavior can be interpreted as a result of the limitation in the grain size D by increasing concentration of Ce^{3+}. The coercivity values for the samples lie in the range of (411–1600 G) and suggest that the investigated materials are potential candidates for sensing, switching, longitudinal and transverse magnetic recording media. Studies of electrical conductivity elucidate a semiconductor to semi-metallic transformation occurring with increasing cerium concentration. The dielectric parameters (tan δ, ε' and ε'') are found to be strongly dependent on composition, temperature, and frequency. Two relaxation processes are designated in these materials as [Fe^{3+}-O^{2-}-Fe^{3+}] and [Co^{2+}-O^{2-}-Co^{2+}] at the octahedral B-sites.

ELECTRONIC SUPPLEMENTARY MATERIAL

The online version of this article (doi: 10.1007/s11664-015-4125-6) contains supplementary material, which is available to authorized users.

REFERENCES

1. M. Hashim, Alimuddin, S. Kumar, B.H. Koo, S.E. Shirsath, E.M. Mohammed, J. Shah, R.K. Kotnala, H.K. Choi, H. Chung, and R. Kumar, *J. Alloys Compd.* 518, 11 (2012).
2. N.G. Imam, S.M. Ismail, M. Yehia, and A. Hashhash, *Int. J. Nanopart.* 7, 170 (2014).
3. M. Hashim, Alimuddin, S.E. Shirsath, S. Kumar, R. Kumar, A.S. Roy, J. Shah, and R.K. Kotnala, *J. Alloys Compd.* 549, 348 (2013).
4. V. Verma, R.K. Kotnala, V. Pandey, P.C. Kothari, L. Radhapiyari, and B.S. Matheru, *J. Alloys Compd.* 466, 404 (2008).
5. T.J. Shinde, A.B. Gadkari, and P.M. Vasambekar, *J. Alloys Compd.* 513, 80 (2012).
6. M.F. Al-Hilli, S. Li, and K.S. Kassim, *J. Magn. Magn. Mater.* 324, 873 (2012).
7. G. Dixit, J. PalSingh, R.C. Srivastava, and H.M. Agrawal, *J. Magn. Magn. Mater.* 324, 479 (2012).
8. M.S. Khandekar, N.L. Tarwal, I.S. Mull, and S.S. Suryavanshi, *Ceram. Int.* 40, 447 (2014).
9. M.A. Malana, R.B. Qureshi, M.N. Ashiq, and Z.I. Zafar, *Mater. Res. Bull.* 48, 4775 (2013).
10. G. Mustafa, M.U. Islam, W. Zhang, Y. Jamil, A.W. Anwar, M. Hussain, and M. Ahmad, *J. Alloys Compd.* 618, 428 (2015).
11. W.D. Penwell and J.B. Giorgi, *Sens. Actuators B* 191, 171 (2014).
12. G. Ennas, M.F. Casula, A. Falqui, D. Gatteschi, G. Marongiu, S. Marras, G. Piccaluga, and C. Sangregorio, *J. Sol-Gel. Sci. Technol.* 26, 463 (2003).
13. B.D. Cullity, *Elements of X-Ray-Diffraction*, 2nd ed, (New York: Addison Wesley Publishing, Co., 1978), vol. 89, pp. 42–46, (pp. 92–102).
14. A.A. Rodríguez-Rodríguez, O.S. Rodríguez-Fernández, J.G.O. Alarcón, and S.M. Montemayor, *J. Sol-Gel. Sci. Technol.* 61, 534 (2012).
15. G. Mustafa, M.U. Islam, W. Zhang, Y. Jamil, M.A. Iqbal, M. Hussain, and M. Ahmad, *J. Magn. Magn. Mater.* 378, 409 (2015).
16. S. Kuai, Z. Zhang, and Z. Nan, *J. Hazard. Mater.* 250, 229 (2013).
17. E.R. Kumar, R. Jayaprakash, and S. Kumar, *J. Magn. Magn. Mater.* 351, 70 (2014).
18. S. Thankachan, B.P. Jacob, S. Xavier, and E.M. Mohammed, *J. Magn. Magn. Mater.* 348, 140 (2013).
19. P. Thangaraj, J. Rajan, S. Durai, S. Kumar, A.R. Phani, and G. Neri, *Vacuum* 86, 140 (2011).
20. H.M. Zaki, S.H. Al-Heniti, and T.A. Elmosalami, *J. Alloys Compd.* 633, 104 (2015).
21. A. Dogra, M. Singh, N. Kumar, P. Sen, and R. Kumar, *Nucl. Instrum. Methods Phys. Res. Sect. B* 212, 190 (2003).
22. M. Yehia, S.M. Ismail, and A. Hashhash, *J. Supercond. Novel Magn.* 27, 771 (2014).
23. M.A. Amer, T.M. Meaz, S.S. Attalah, and A.I. Ghoneim, *J. Magn. Magn. Mater.* 363, 60 (2014).
24. A.B. Gadkari, T.J. Shinde, and P.N. Vasambekar, *J. Magn. Magn. Mater.* 322, 3823 (2010).
25. M.A. Gabal, R.S. Al-luhaibi, and Y.M. Al-Angari, *J. Hazard. Mater.* 246, 227 (2013).
26. J.B. Goodenough, *Phys. Rev.* 117, 1442 (1960).
27. A. Hashhash, M. Kaiser, and S.S. Ata-allah, *J. Supercond. Novel Magn.* 28, 2193 (2015).
28. M.A. Ahmed, S.T. Bishay, R.M. Khafagy, and N.M. Saleh, *J. Magn. Magn. Mater.* 350, 73 (2014).
29. A.A. Satter and K.M. El-shokrofy, *J. Phys. IV* 7, 245 (1997).
30. J.S. Zheludev, *Physics of Crystalline Dielectrics, Electrical Properties*, Vol. 2 (New York: Plenum Press, 1971)), p. 517.
31. M.M. El-Ocker, M.A. Mostafa, H.M.T. Aly, R.L. Mohamed, and A.S.T. Saadoun, *Phys. Status Solidi (a).* 158, 205 (1996).
32. N. Rezlescu and E. Rezlescu, *Solid State Commun.* 14, 69 (1974).
33. R.K. Selvan, C.O. Augustin, V. Sepelak, L.J. Berchmans, C. Sanjeeviraja, and A. Gedanken, *Mater. Chem. Phys.* 112, 373 (2008).
34. L.J. Berchmans, R.K. Selvan, and C.O. Augustin, *Mater. Lett.* 58, 1928 (2004).
35. N. Rezlescu, C. Prakash, and G. Prasad, *J. Phys. D* 39, 1635 (2006).
36. M.M. El-sayed, *Ceram. Int.* 33, 314 (2007).
37. A. Hashhasha, N.G. Imam, S.M. Ismaila, and M. Yehia, *J. Electron. Mater.* 44, 3833 (2015).